

CrossMark  
click for updatesCite this: *RSC Adv.*, 2015, 5, 86941Received 29th July 2015  
Accepted 9th October 2015

DOI: 10.1039/c5ra15108b

www.rsc.org/advances

## ZnS nanoparticles embedded in porous carbon matrices as anode materials for lithium ion batteries†

Yun Fu, Zhian Zhang,\* Xing Yang, Yongqin Gan and Wei Chen

*In situ* synthesis of a novel zinc sulfide/porous carbon composite (ZnS/PC) with ZnS nanoparticles finely embedded in porous carbon matrices is achieved by virtue of the metal–organic frameworks (MOFs) strategy. The as-obtained ZnS/PC exhibits significant electrochemical performance as an anode material for lithium ion batteries.

Lithium ion batteries (LIBs) have been one of the most promising energy conversion and storage devices due to their environmental friendliness, high energy density, wide working temperature and high voltage.<sup>1–3</sup> However, the achievement of LIBs with remarkable electrochemical performances to meet the increasing requirements, is well known to be limited by the lack of suitable electrochemically active materials. Consequently, a variety of electrode materials such as carbon, metal, and metallic compound have been actively studied as potential application for Li<sup>+</sup> storage.<sup>4–14</sup> In particular, Zn-based materials have been researched as one of the alternative anode materials due to their natural abundance, cost-effective, as well as environmental friendliness and high theoretical capacities. Among Zn-based binary compounds, ZnO,<sup>15</sup> ZnSe,<sup>16</sup> Zn<sub>4</sub>Sb<sub>3</sub>,<sup>17</sup> ZnSb,<sup>18</sup> ZnP<sub>2</sub>,<sup>19</sup> have been evaluated and show promising electrochemical performance. As an important Zn-based compound, zinc sulfide also has been investigated in LIBs application.<sup>13,16,20</sup> However, the practical Li<sup>+</sup> storage capabilities of ZnS is accompanied by the inherent unsatisfied electrical conductivity and large volume change upon Li<sup>+</sup> insertion–extraction process, resulting in the pulverization of ZnS-based electrodes and the limited cycle performances.<sup>12,21</sup> Consequently, rational design of ZnS-based anode materials with facile synthesis to address these problems is urgent and some attempt has been done. For example, ZnS/C composites were prepared by a combined precipitation with carbon coating method and exhibited superior performance with 304 mA h g<sup>−1</sup> after 300 cycles at 400 mA g<sup>−1</sup>.<sup>13</sup> Mao *et al.*

synthesized ZnS/graphene composites using solvothermal process, which effectively improved the properties of ZnS and demonstrated excellent cycle ability.<sup>22</sup> Among various strategies, for purpose of enhancing the performance of energy storage, constructing hybrid materials of ZnS with conductive carbonaceous support and fabricating embedded nanoparticles within a conductive matrix to accommodate volume change, keep the integrity of the electrode structure and improve conductivity still need more efforts.

Currently, metal–organic frameworks (MOFs) have attracted particular attention in gas storage, separations, catalysis and energy storage as novel nanoporous materials.<sup>23,24</sup> Inspired by properties of controllable structures, huge surface area, tunable pore size and high porosity, MOFs have also been considered as an alternative precursor to construct metal-based nano-architecture materials.<sup>25–28</sup> For instance, Co<sub>3</sub>O<sub>4</sub> nanoparticles have been prepared by pyrolysed cobalt-MOF at 800 °C and provide a stable Li<sup>+</sup> storage capacity of 965 mA h g<sup>−1</sup> after 50 cycles at 50 mA g<sup>−1</sup>.<sup>26</sup> A heat treatment of a well-known metal–organic framework of MOF-5 yields ZnO@carbon, which can contain a stable capacity of 335 mA h g<sup>−1</sup> up to the 50th cycle at 100 mA g<sup>−1</sup>.<sup>27</sup> More recently, Wang *et al.*<sup>28</sup> prepared CoS<sub>2</sub>/carbon composite with ultrasmall CoS<sub>2</sub> nanoparticles finely embedded in thin N-rich porous carbon by using ZIF-67 templates, showing promising Li<sup>+</sup> storage properties with negligible loss of capacity at high charge/discharge rate.

In this work, we extended the application of the MOFs strategy to facile synthesize zinc sulfide/porous carbon composite (ZnS/PC) with ZnS nanoparticles embedded in porous carbon matrices. MOF-5 was chosen as the MOF precursor because it is amenable to mass production, it has excellent purity and high crystallinity.<sup>29</sup> The obtained composites possess large surface area and porous structure, excellent conductive carbon matrix, and the robust integration between ZnS nanoparticles and carbon frameworks. Such a hybrid structure can offer enough space to buffer the volume expansion of ZnS nanoparticles during Li<sup>+</sup> intercalation and deintercalation process, provide remarkable conductive network, shorter lengths of electronic

School of Metallurgy and Environment, Central South University, Changsha, Hunan 410083, China. E-mail: zza75@163.com; Tel: +86 731 88830649

† Electronic supplementary information (ESI) available: Synthetic methods and experimental data of carbonized MOF-5 precursor. See DOI: 10.1039/c5ra15108b

path, and more contact pathways between electrolyte and ZnS particles within carbon matrix. When evaluated as an electrochemically active material for LIBs, the as-obtained ZnS/PC exhibited significant electrochemical performance with a reversible capacity of  $438 \text{ mA h g}^{-1}$  in 300 cycles at  $100 \text{ mA g}^{-1}$ .

The morphologies and microstructures of the as-prepared ZnS/PC have been investigated with FESEM and TEM as shown in Fig. 1. The result reveals that ZnS/PC retains the cubic structure in which ZnS nanoparticles with less than  $120 \text{ nm}$  were embedded after hydrothermal sulfidation (Fig. S1†). The high-resolution TEM image in Fig. 1c shows an interlayer distance of  $0.32 \text{ nm}$ , which agrees well with the space (111) planes of ZnS crystals. Furthermore, the embedded structure is further proven by the distribution of C, S, and Zn elements from energy dispersive spectrometer (EDS) mapping (Fig. 1d).

Fig. 2a presents the XRD patterns of ZnS/PC and pure ZnS, where all of the diffraction peaks of pure ZnS can be indexed to a cubic ZnS phase (JCPDS no. 65-9585). Compared with pure ZnS, the ZnS/PC has an extra weak peak at  $27^\circ$ , which belongs to hexagonal ZnS phase (JCPDS no. 36-1450). Additionally, there was no other impurity peaks are observed from the XRD patterns, indicating a complete conversion of ZnO to ZnS. The energy-dispersive X-ray (EDX) spectroscopy as shown in Fig. 2b reveals that the atomic ratio of Zn/S approaches to 1 : 1, which corresponds to the stoichiometric ratio of the compound of ZnS. In order to confirm the mass percentage of ZnS in the composites, TGA was employed at a heating rate of  $10^\circ \text{C min}^{-1}$  in dry air. The

TGA profiles of ZnS/PC, pure ZnS and carbonized MOF-5 is shown in Fig. 3a. The mass loss below  $300^\circ \text{C}$  could be ascribed to the evaporation of absorbed water. Comparing the TGA profiles of ZnS/PC and pure ZnS, it can be concluded that the weight loss from  $300$  to  $520^\circ \text{C}$  on the TGA profile of ZnS/PC was attributed to the combustion of carbon,<sup>30</sup> which had no relation with the oxidation of ZnS, the other obvious weight loss, which arises between  $520$  and  $640^\circ \text{C}$ , corresponds to oxidation of ZnS to ZnO.<sup>22</sup> Therefore, the carbon content was calculated as  $(98\% - 77.5\%)/98\% = 20\%$ . From the TGA profile of carbonized MOF-5, it also can calculate the carbon content in ZnS/PC is  $20\%$  (the detailed analysis is listed in ESI†). To investigate the porous structure of the ZnS/PC,  $\text{N}_2$  adsorption-desorption analysis was performed at  $77 \text{ K}$  and shown that ZnS/PC possessed a large surface area of  $296.8 \text{ m}^2 \text{ g}^{-1}$  (Fig. 3b), which could provide a large interface to enhance the contact between electrolyte and active material, and facilitate the electrochemical reaction.<sup>6</sup> The pore volume of  $0.318 \text{ cm}^3 \text{ g}^{-1}$  and the pores of most size less than  $10 \text{ nm}$ , as derived by using the Barrett-Joyner-Halenda (BJH) method, are also beneficial for buffering the volume change during  $\text{Li}^+$  intercalation and deintercalation process.

The electrochemical performances of lithium ion storage based on the as-prepared materials were first evaluated by cyclic voltammograms (CV) and galvanostatic charge-discharge curves. Fig. 4a displays the first three cyclic voltammograms of ZnS/PC at a scanning rate of  $0.02 \text{ mV s}^{-1}$ . In the first scanning cycle, several weak reduction peaks, which appear below  $0.8 \text{ V}$ , are related with the reduction of ZnS to metallic zinc and the further formation of Zn-Li alloys with multiple steps (such as  $\text{LiZn}_4$ ,  $\text{Li}_2\text{Zn}_5$ ,  $\text{LiZn}_2$ ,  $\alpha\text{-Li}_2\text{Zn}_3$  and  $\text{LiZn}$ ).<sup>20</sup> The basic reactions during positive scan are elucidated by the eqn (1) and (2).<sup>13,20,22</sup> Solid electrolyte interface (SEI) layer might also form on the surface of electrode owing to the reductive decomposition of electrolyte during the first scanning process, which caused part of the irreversible capacity.<sup>2,13</sup> During the cathode scan, three small oxidation peak observed in the potential range of  $0.01$ – $0.7 \text{ V}$  correspond to the dealloying process of Li-Zn alloys, which is also a multi-step process. The next oxidation peak at  $1.3 \text{ V}$  is attributed to the reconstruction of ZnS from Zn and  $\text{Li}_2\text{S}$ . Fig. 4b reveals the typical galvanostatic discharge-charge (GDC) curves of the ZnS/PC over the potential range between  $0.01 \text{ V}$  and  $2.5 \text{ V}$  at a constant current density of  $100 \text{ mA g}^{-1}$ . It is observed that the plateaus of GDC curves correspond to the CV peaks

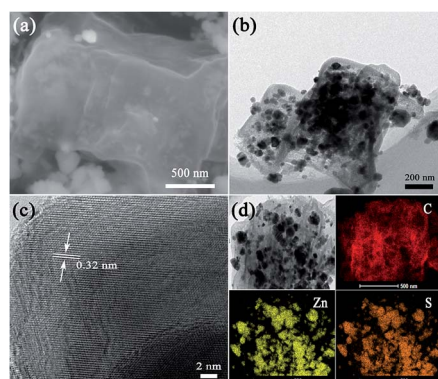


Fig. 1 (a) FESEM image; (b) TEM image; (c) HRTEM image and (d) elemental mapping images of ZnS/PC.

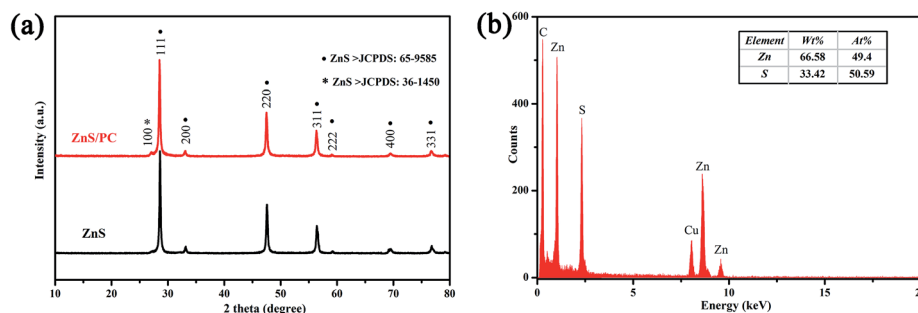


Fig. 2 (a) XRD patterns of ZnS/PC and pure ZnS, (b) EDX spectroscopy of ZnS/PC.

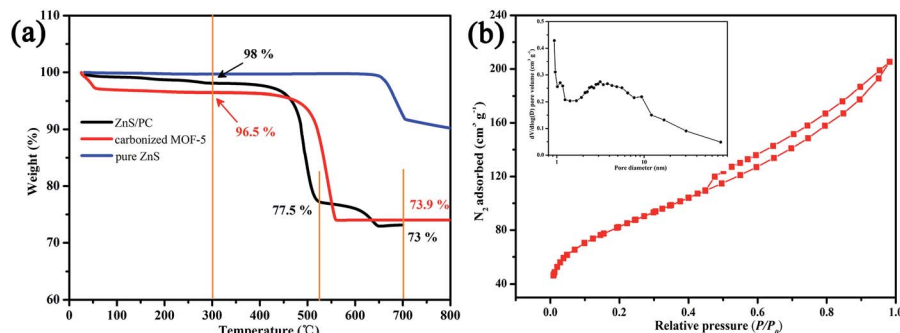
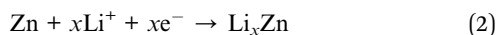
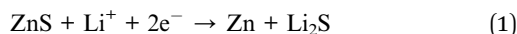


Fig. 3 (a) TGA curves of ZnS/PC, pure ZnS and carbonized MOF-5, (b) N<sub>2</sub> sorption isotherms measured at 77 K of ZnS/PC. The inset in (b) shows the pore-size distribution calculated using the BJH method.

in Fig. 4a. Upon the initial discharge, the ZnS/PC display a discharge capacity of 1220 mA h g<sup>-1</sup>, which is close to the previous reports.<sup>13,22</sup> The large initial capacity may attribute to the well utilization of active material and the irreversible formation of the SEI film on the surface of the composite. Owing to the high specific surface, an excessive interface between the active material and electrolyte may lead to more considerable side reactions related with SEI, which provides more irreversible capacity. From the 2nd cycle onwards, the composite delivers discharge capacities of 680, 580, 470, 480 mA h g<sup>-1</sup> in the 2nd, 3rd, 20th and 50th cycle respectively.



To further evaluate the electrochemical properties of the ZnS/PC and verify the superiority of carbon framework, the cycle

behaviors of ZnS/PC and pure ZnS at 100 mA g<sup>-1</sup> were tested as shown in Fig. 4c. Note that all the capacity values of ZnS/PC were calculated based on the total mass of the composite. After 300 cycles, the composite maintains a reversible capacity of 438 mA h g<sup>-1</sup> with a stable coulombic efficiency nearly 100%, indicating the good reversibility of the Li<sup>+</sup> intercalation and deintercalation processes, while the pure ZnS only delivers 220 mA h g<sup>-1</sup> after 80 cycles. The significant improved electrochemical performance of ZnS/PC should be attributed to rational nanostructure of the composite. In virtue of sufficient space, ZnS nanoparticles embedded in porous carbon matrices can better adapt the volume change arising from the charge-discharge processes, thus avoiding the pulverization problem efficiently, which can keep the structural integrity. Meanwhile, the large surface area and porous structure of the ZnS/PC not only provide shorter path lengths for lithium ion and electronic but also offer more electrolyte pathways to the inside ZnS nanoparticles through the carbon matrix. The capability of the

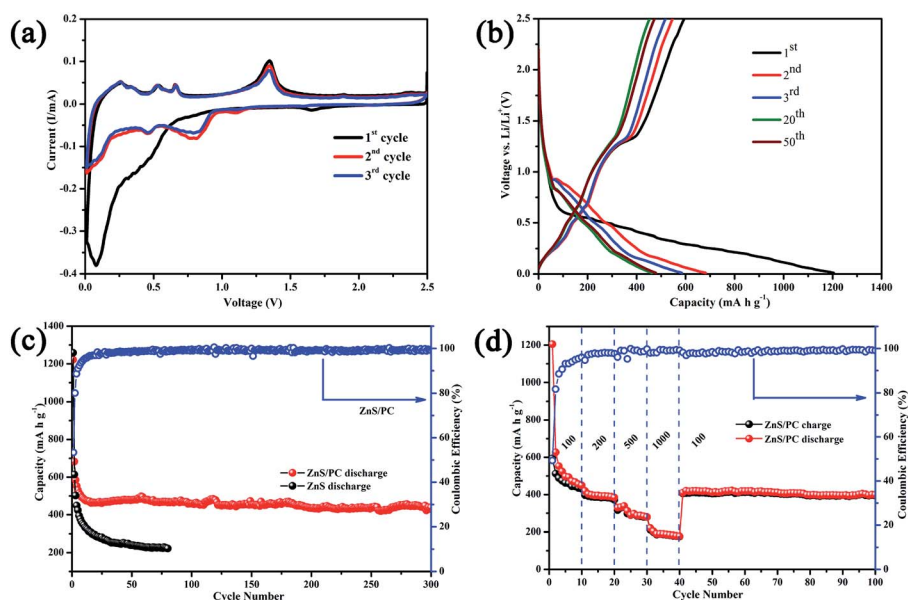


Fig. 4 (a) Cyclic voltammograms of the ZnS/PC, (b) charge-discharge curves of the ZnS/PC, (c) cycling property of the ZnS/PC and pure ZnS at 100 mA g<sup>-1</sup> and (d) the capability of the ZnS/PC at various current densities.

ZnS/PC at various current densities was evaluated and shown in Fig. 4d. Upon gradually elevating the current density, a capacity  $180 \text{ mA h g}^{-1}$  is retained at  $1000 \text{ mA g}^{-1}$  (Fig. 4d). When the current density decreases to  $100 \text{ mA g}^{-1}$  after cycling with high current densities, the discharge capacity can recover to the original value immediately, indicating that the as-synthesized ZnS/PC possesses well structure stability even under high rate cycling.

In summary, a MOF-derived synthesis strategy to prepare ZnS/PC with ZnS nanoparticles embedded in porous carbon matrices has been developed. The obtained composite possess large surface area and porous structure, excellent conductive carbon matrix, and robust integration of ZnS nanoparticles and carbon frameworks. The rational design of such composite structure can be expected to develop advanced electrode materials. When evaluated as an anode material for LIBs, the as-obtained ZnS/PC exhibited excellent electrochemical performance with a reversible capacity of  $438 \text{ mA h g}^{-1}$  in 300 cycles at  $100 \text{ mA g}^{-1}$ . The results demonstrate the advantage of the MOF-derived ZnS/PC structures, and further provide help for developing electrode materials with high performance applications in lithium ion batteries.

## Acknowledgements

This work is supported by the Fundamental Research Funds for the Central Universities of Central South University (2015zzts187).

## References

- 1 Y. Gong, S. Yang, Z. Liu, L. Ma, R. Vajtai and P. M. Ajayan, *Adv. Mater.*, 2013, **25**, 3979–3984.
- 2 X. Wang, Q. Xiang, B. Liu, L. Wang, T. Luo, D. Chen and G. Shen, *Sci. Rep.*, 2013, **3**, 2007.
- 3 S.-K. Park, S. Woo, S. Lee, C.-Y. Seong and Y. Piao, *RSC Adv.*, 2015, **5**, 52687–52694.
- 4 G. Li, L. Xu, Q. Hao, M. Wang and Y. Qian, *RSC Adv.*, 2012, **2**, 284–291.
- 5 G. Zhang, S. Hou, H. Zhang, W. Zeng, F. Yan, C. C. Li and H. Duan, *Adv. Mater.*, 2015, **27**, 2400–2405.
- 6 R. Wu, D. P. Wang, X. Rui, B. Liu, K. Zhou, A. W. Law, Q. Yan, J. Wei and Z. Chen, *Adv. Mater.*, 2015, **27**, 3038–3044.
- 7 C. Zhu, Y. Wen, P. A. van Aken, J. Maier and Y. Yu, *Adv. Funct. Mater.*, 2015, **25**, 2335–2342.
- 8 S. Liu, X. Lu, J. Xie, G. Cao, T. Zhu and X. Zhao, *ACS Appl. Mater. Interfaces*, 2013, **5**, 1588–1595.
- 9 C. Villevieille, X.-J. Wang, F. Krumeich, R. Nesper and P. Novák, *J. Power Sources*, 2015, **279**, 636–644.
- 10 W. Chen, T. Li, Q. Hu, C. Li and H. Guo, *J. Power Sources*, 2015, **286**, 159–165.
- 11 K. Shiva, H. S. S. Ramakrishna Matte, H. B. Rajendra, A. J. Bhattacharyya and C. N. R. Rao, *Nano Energy*, 2013, **2**, 787–793.
- 12 G. D. Park, S. H. Choi, J. K. Lee and Y. C. Kang, *Chemistry*, 2014, **20**, 12183–12189.
- 13 L. He, X.-Z. Liao, K. Yang, Y.-S. He, W. Wen and Z.-F. Ma, *Electrochim. Acta*, 2011, **56**, 1213–1218.
- 14 Y. Xu, J. Feng, X. Chen, K. Kierzek, W. Liu, T. Tang and E. Mijowska, *RSC Adv.*, 2015, **5**, 28864–28869.
- 15 S. Li, Y. Xiao, X. Wang and M. Cao, *Phys. Chem. Chem. Phys.*, 2014, **16**, 25846–25853.
- 16 H.-T. Kwon and C.-M. Park, *J. Power Sources*, 2014, **251**, 319–324.
- 17 J. Xu, H. Wu, F. Wang, Y. Xia and G. Zheng, *Adv. Energy Mater.*, 2013, **3**, 286–289.
- 18 S. Saadat, J. Zhu, M. M. Shahjamali, S. Maleksaeedi, Y. Y. Tay, B. Y. Tay, H. H. Hng, J. Ma and Q. Yan, *Chem. Commun.*, 2011, **47**, 9849–9851.
- 19 C.-M. Park and H.-J. Sohn, *Chem. Mater.*, 2008, **20**, 6319–6324.
- 20 Y. Hwa, J. H. Sung, B. Wang, C.-M. Park and H.-J. Sohn, *J. Mater. Chem.*, 2012, **22**, 12767.
- 21 X. Rui, H. Tan and Q. Yan, *Nanoscale*, 2014, **6**, 9889–9924.
- 22 M. Mao, L. Jiang, L. Wu, M. Zhang and T. Wang, *J. Mater. Chem. A*, 2015, **3**, 13384–13389.
- 23 H. Furukawa, K. E. Cordova, M. O'Keeffe and O. M. Yaghi, *Science*, 2013, **341**, 1230444.
- 24 W. Chaikittisilp, K. Ariga and Y. Yamauchi, *J. Mater. Chem. A*, 2013, **1**, 14–19.
- 25 F.-S. Ke, Y.-S. Wu and H. Deng, *J. Solid State Chem.*, 2015, **223**, 109–121.
- 26 B. Liu, X. Zhang, H. Shioyama, T. Mukai, T. Sakai and Q. Xu, *J. Power Sources*, 2010, **195**, 857–861.
- 27 H. Yue, Z. Shi, Q. Wang, Z. Cao, H. Dong, Y. Qiao, Y. Yin and S. Yang, *ACS Appl. Mater. Interfaces*, 2014, **6**, 17067–17074.
- 28 Q. Wang, R. Zou, W. Xia, J. Ma, B. Qiu, A. Mahmood, R. Zhao, Y. Yang, D. Xia and Q. Xu, *Small*, 2015, **11**, 2511–2517.
- 29 S. J. Yang, S. Nam, T. Kim, J. H. Im, H. Jung, J. H. Kang, S. Wi, B. Park and C. R. Park, *J. Am. Chem. Soc.*, 2013, **135**, 7394–7397.
- 30 X. Meng, S. C. Riha, J. A. Libera, Q. Wu, H.-H. Wang, A. B. F. Martinson and J. W. Elam, *J. Power Sources*, 2015, **280**, 621–629.